In-situ interferometric monitoring of optical coatings

Séverin L Nadji, Michel Lequime, Thomas Begou, Cihan Koc, Catherine Grèzes-Besset, Julien Lumeau

In-situ interferometric monitoring of optical coatings

SÉVERIN L. NADJI,[1,3] MICHEL LEQUIME,[1,*] THOMAS BEGOU,[1] CIHAN KOC,[1] CATHERINE GRÈZES-BESSET,[2] AND JULIEN LUMEAU[1]

[1] *Aix Marseille Univ, CNRS, Centrale Marseille, Institut Fresnel, Marseille, France*
[2] *CILAS Ariane Group, 600 Avenue de la RocheFourcade, ZI St Mitre, 13400 Aubagne, France*
[3] *Currently with Max-Planck Institut fur Gravitationsphysik (Albert Einstein Institut), 30167, Hannover, Germany*
[*] *michel.lequime@fresnel.fr*

Abstract: We present a new method for the *in situ* measurement of the amplitude and phase of the reflection coefficient of a plane substrate installed in a mechanical holder rotating at high speed (120 turns per minute) during the deposition of an optical thin-film stack. Our method is based on digital holography and uses a self-referenced scheme to cancel the effects of the severe constraints generated by the vibrational and thermal environment of the deposition machine.

1. Introduction

The realization of complex optical filtering functions requires perfect control of the deposition process as well as accurately monitoring the thicknesses of the deposited layers in real time. Existing techniques are based on physical or optical methods, the principle consisting in the latter case of following the change in transmittance T (or the reflectance R) of a witness sample during the stack deposition. If this measurement is made at a single wavelength, one talks of monochromatic monitoring, otherwise when this measurement is made over a wide spectral range, the method is defined as broadband monitoring [1].

All these optical methods are based on intensity measurements, and consequently the phase information, which is a critical parameter in a multiple-wave interference phenomenon such as that involved within a multi-layer stack, is totally lost. Some studies [2–4] have shown that it is possible to make an interferometric measurement of the stack properties in the noisy environment of a deposition machine by using *Dynamic Interferometry*®. This technique, developed and patented by 4D Technology [5], implements a micro-polarizer pixelated camera to achieve the instantaneous acquisition of four different phase states of the field reflected by the sample [6]. It is clearly a very efficient solution, but quite expensive and requires a contractual agreement with 4D Technology to use their patented sensor (PolarCam™) within an interferometric set-up. Moreover, a tunable retarder is used together with a low coherence source to record only the result of the interference between the fields reflected by the coated front face and by the uncoated rear face, used here as a reference surface [2]. This means that the measurement is sensitive to any phase variations between these two surfaces, such as that induced by a temperature change in the witness glass.

These are the main reasons why we have chosen to develop an alternative approach using a self-referenced interferometric configuration, in which the phase information is obtained by digital holography processing [7]. In section 2, we first present the main characteristics of the deposition machine, the self-referenced scheme we implemented for the substrate as well as the structure of the interferometric measurement set-up. Section 3 is devoted to the presentation of a theoretical model that predicts the temporal change in the data provided by the interferometric set-up throughout the deposition of single layers (high index and low index), but also provides a detailed description of the data processing used to extract the modulus and phase of the

reflection coefficient. In Section 4, we present the main experimental results obtained with this interferometric configuration and we analyze the agreement between the recorded phase information and the predictions of our theoretical model. Finally, we conclude and define the possible applications of our method (Section 5).

2. Materials and Methods

2.1. Deposition machine

The deposition machine uses a dual ion beam sputtering technique (DIBS) to obtain dense layers of high purity oxides. Figure 1 illustrates the inside of the vacuum chamber showing three planar targets of silicon, tantalum, and hafnium mounted on a rotating mechanism. Each material is deposited by sputtering the surface of the corresponding target with a highly energetic argon ion beam (not visible in the picture) in a reactive oxygen atmosphere. During the growth of the layers, a second lower-energy ion beam, mixing argon and oxygen, is directed towards the sample to adjust the stoichiometry of each oxide layer (SiO_2, Ta_2O_5, HfO_2) and improve their packing density.

Fig. 1. The DIBS deposition machine (on the left, schematic view of the substrate configuration; on the right, picture of the inside of the machine).

The sample to be coated is a plane silica window 25 mm in diameter, 1 or 2 mm thick, installed in a rotating substrate holder, as shown on the left of Figure1. The rotary movement of the substrate (rotation speed 120 turns per minute) is used to improve the uniformity of the layers deposited at the bottom surface of this sample. This sample can be illuminated with a collimated probe beam from the top of the machine through the entrance window, and this beam is shifted sideways by a periscope. This probe beam is thus fixed relative to the machine, which means that it is necessary to synchronize any transmission or reflection measurement with the rotation of the substrate holder [8].

2.2. Measurement system

The design of the interferometric measurement system must take into account three main constraints, namely:

1. a continuous displacement of the sample with respect to the machine frame, which can be caused by thermal expansion of the chamber and wobbling of the substrate holder,
2. the vibration of the machine caused by the vacuum pump,
3. the presence of a parasitic signal due to the reflection of the probe light beam from the top face of the substrate.

To overcome the first constraint, we insert a very thin plane steel ring between the bottom face of the substrate and the substrate holder, as shown in Figure 2. This annular stop prevents the deposition of any material onto the outer zone of the substrate, and this uncoated circular crown can be used as a local reference for the interferometric measurement of the layer thickness deposited over the central zone. Consequently, the result of a measurement is the difference $\Delta\phi$ between the phase values recorded at the center (ϕ_C) and in the outer annular zone (ϕ_A) respectively of the substrate.

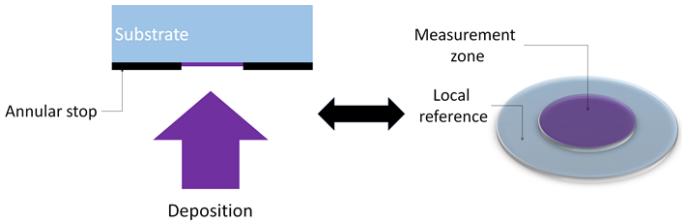

Fig. 2. Principle of the substrate self-referencement.

To solve the vibrations problem, we used a powerful light source working in triggered mode, synchronized to the substrate holder rotation (2 Hz) and emitting a very short pulse (10 μs), allowing an instantaneous interference state when the witness sample is centered on the probe beam to be recorded. Spurious interference signals are suppressed in the same way as that implemented by Lee et al. [2], namely the use of a low coherence source.

We installed on the top of the deposition machine a high stiffness optical bench holding a Michelson type interferometer with one arm formed by the periscope-substrate assembly, as shown in Figure 3. A low coherence source (superluminescent diode, central wavelength $\lambda_0 = 830$ nm, spectral bandwidth $\Delta\lambda = 17$ nm) is coupled into a single mode fiber whose output end is placed in the focal plane of an aspherical lens with a focal length of 150 mm. The collimated beam provided by this assembly is divided into two perpendicular arms by a cube beam splitter. The light beam transmitted by the splitter (reference beam) is reflected by a plane mirror mounted on a motorized translation stage, while the beam reflected downwards by the same beam splitter (probe beam) illuminates the whole surface of the witness substrate after passing through the periscope. Both reflected beams are recombined by the splitter cube and detected by a low-noise 14-bit CCD camera with 1600×1200 pixels of 7.4 μm square. Finally, a low-distortion photographic lens is used to image the bottom surface of the witness sample on this CCD matrix.

A small tilt is introduced between the two end-mirrors of the Michelson interferometer, in order to produce a quasi-parallel fringes pattern at the surface of the CCD, as shown in Figure 4.

To ensure a good quality recording of this fringe pattern by the CCD matrix, it is first necessary for the pixel size p to be not greater than one sixth of the fringe period P, i.e.

$$p \leqslant \frac{P}{6} = \frac{\lambda_0}{12\,\theta} \tag{1}$$

where θ is the instantaneous value of the tilt angle between the two end-mirrors. This leads a maximum tilt angle of approximately 10 milliradians (0.6 degree) to be specified between the two

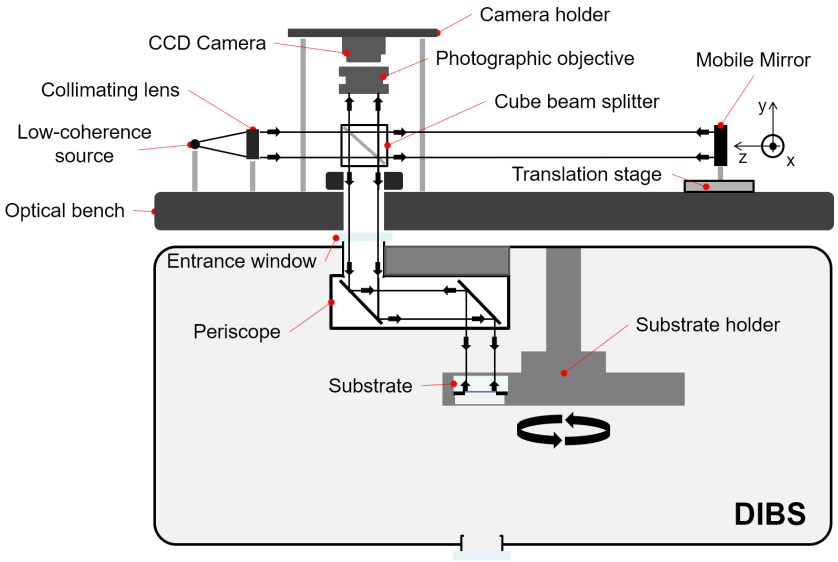

Fig. 3. Schematic representation of the interferometric set-up installed on the top of the DIBS vacuum chamber.

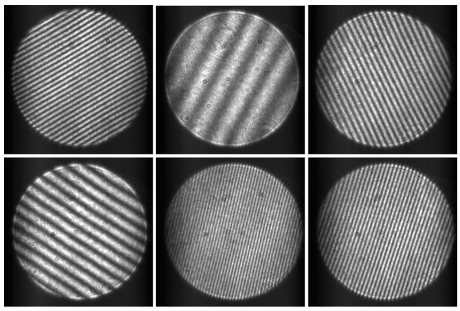

Fig. 4. Examples of interferograms recorded by the CCD camera on a mirror sample.

end-mirrors of the Michelson interferometer. However, this fringe pattern must also be recorded with good contrast, which requires that the changes of the relative axial position between these two end-mirrors be less than half the coherence length l_c of the source, i.e.

$$\delta z \leqslant \frac{l_c}{2} = \frac{\lambda_0^2}{2\Delta\lambda} \sim 20\,\mu\text{m} \tag{2}$$

To relax this axial stability constraint up to 100 μm, while maintaining the benefits of the low coherence interferometric scheme, an additional bandpass filter (central wavelength 830 nm, spectral bandwidth 3.2 nm) is placed in front of the CCD camera; furthermore, this filter reduces the amount of parasitic light seen by the CCD matrix.

3. Theoretical model

3.1. Reflection coefficient

As emphasized in Section 2.2, the result of a measurement is the difference between the phase values recorded in the central zone C and the annular zone A, i.e. to a first approximation,

$$\Delta\phi = \phi_C - \phi_A = \rho_c - \rho_A \tag{3}$$

where ρ is the phase of the reflection coefficient r, defined as

$$r = \sqrt{R}\, e^{i\rho} \tag{4}$$

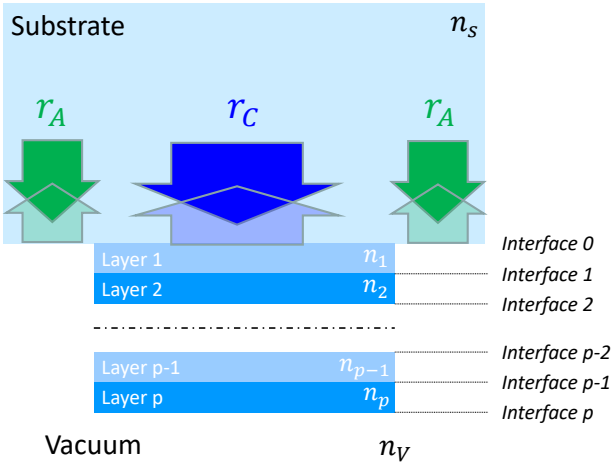

Fig. 5. Schematic view of the measurement method.

Figure 5 gives a schematic view of the measurement method. For the reference zone A, the reflection coefficient is given by:

$$r_A = \frac{n_s - 1}{n_s + 1} \tag{5}$$

where $\tilde{n}_s$ is the effective index of the substrate. Consequently: $\rho_A = 0$.

Similarly, for the central zone C, the reflection coefficient is given by [9, 10]:

$$r_C = \frac{\tilde{n}_s - Y_0}{\tilde{n}_s + Y_0} \tag{6}$$

where Y_0 is the complex admittance of the bottom interface of the substrate (i.e. the top interface of the stack). For example, in the case of a single layer, we have

$$r_C = \frac{n_1(n_s - n_v)\cos\delta_1 - i(n_s n_v - n_1^2)\sin\delta_1}{n_1(n_s + n_v)\cos\delta_1 - i(n_s n_v + n_1^2)\sin\delta_1} \tag{7}$$

which leads to the following expression for the phase ρ_C:

$$\rho_C = \arctan\left[\frac{2n_s n_1(n_1^2 - n_v^2)\sin 2\delta_1}{(n_1^2 + n_v^2)(n_s^2 - n_1^2) + (n_1^2 - n_v^2)(n_s^2 + n_1^2)\cos 2\delta_1}\right] \tag{8}$$

Figure 6 shows the variation of the phase difference $\Delta\phi = \rho_C - \rho_A$ versus the thickness of the deposited layer, on the left for SiO_2 and on the right, for Ta_2O_5. Note that the non-linearity of

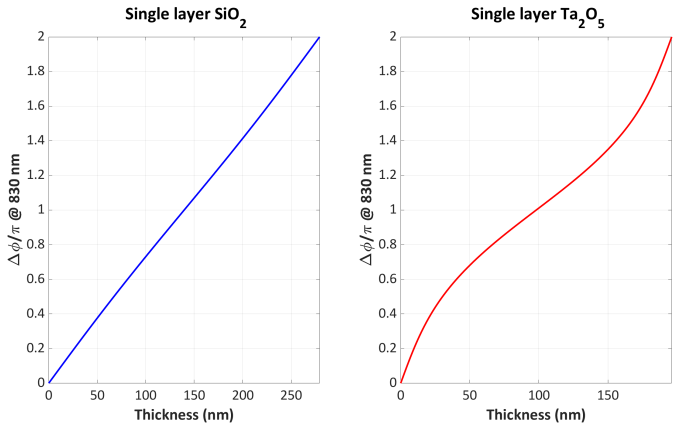

Fig. 6. Theoretical variation of the phase difference $\Delta\phi$ versus the thickness of the deposited layer (on the left, silica; on the right, tantala).

this relation increases with the mismatch between the refractive index of the layer and that of the substrate. Note also that the deposition of a silica layer onto a silica substrate can be monitored using this interferometric approach even if their refractive indices are identical; this would be impossible in the case of intensity monitoring.

3.2. Data processing

Quite generally, the signal recorded by the CCD matrix is described by the following relation:

$$S(x, y) = S_0(x, y) + S_1(x, y) \cos\left[\frac{4\pi}{\lambda}(\alpha x + \beta y) + \Phi(x, y)\right] \tag{9}$$

where α and β are the components of the tilt angle along x and y axes.

Figure 7a shows a false color representation of this fringe pattern when the central zone of a substrate is coated with a 90 nm thick Ta_2O_5 layer. The surface flatness error of this substrate is roughly λ, causing a slight deformation of the fringes, almost imperceptible on the illustration.

A 2D fast Fourier transform is applied to this digitized signal, resulting in three separate orders (see Figure 7b for a false color representation of this Fourier spectrum in log scale), in accordance with the following expression:

$$\widetilde{S}(f_x, f_y) = \widetilde{S}_0(f_x, f_y) + \widetilde{S}_+(f_x - 2\alpha/\lambda, f_y - 2\beta/\lambda) + \widetilde{S}_-(f_x + 2\alpha/\lambda, f_y + 2\beta/\lambda) \tag{10}$$

where $\widetilde{S}$ is the Fourier transform of S and where $S_\pm(x, y)$ is defined by:

$$S_\pm(x, y) = \frac{1}{2} S_1(x, y) e^{\pm i\Phi(x,y)} \tag{11}$$

Windowing is then applied to this spectrum around the first order (see Figure 7c) and the filtered data are re-centered on the spatial frequency origin (see Figure 7d). Note that the quality of this windowing requires that the ± 1 orders are sufficiently far from the central zero order (tilt angle $\theta > 5$ milliradians).

An inverse 2D fast Fourier transform is applied to this re-centered signal to recover the function $S_+(x, y)$. A modulo 2π determination of the phase $\Phi(x, y)$ is given by

$$\phi(x, y) = \arctan\left\{\frac{\Im[S_+(x, y)]}{\Re[S_+(x, y)]}\right\} \equiv \Phi(x, y) \pmod{2\pi} \tag{12}$$

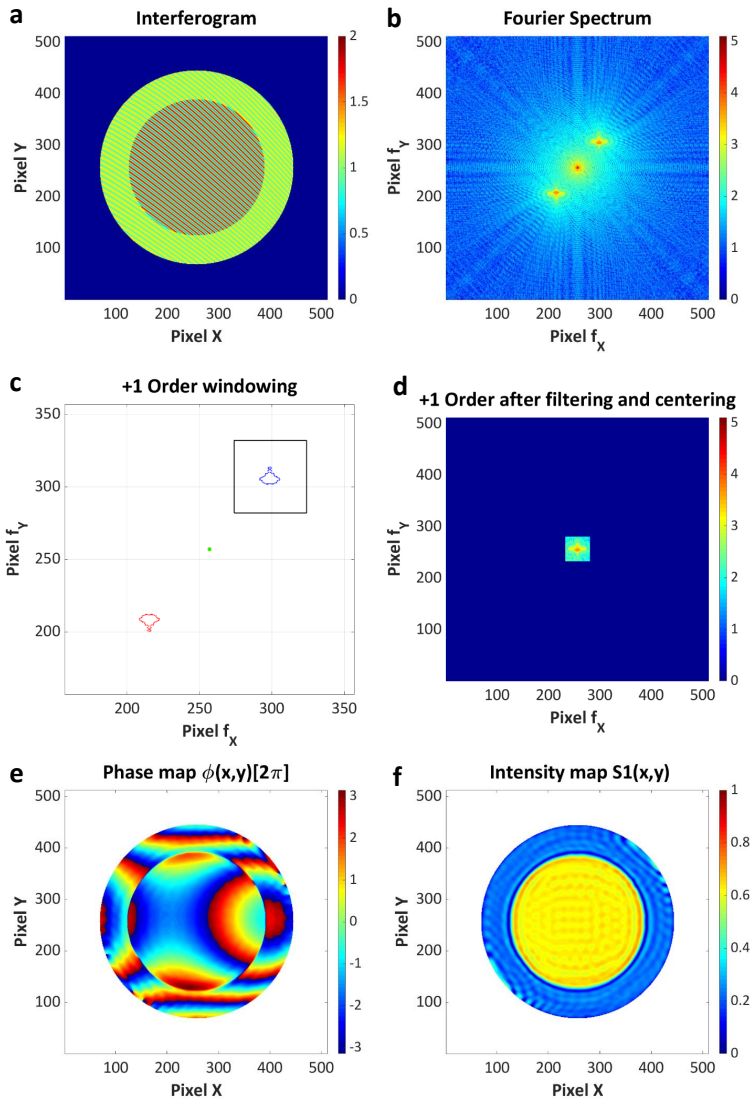

Fig. 7. Numerical modelling of the different steps used for the data processing (see text for more details).

while the modulus of $S_+(x, y)$ is simply equal to $2S_1(x, y)$ (see Figs.7e and 7f respectively). Note in Figure 7f the deformation of the phase map levels caused by the initial surface flatness error of the substrate.

Finally this phase, modulo 2π, is transformed into an absolute value, via a phase unwrapping procedure based on the algorithm developed by Herraez et al. [11]. Some examples of phase maps recorded before and after unwrapping are shown in Figure 8: at the top (graphs a and b) before coating, and in the middle (graphs c and d) after deposition of a half-wave layer of Ta_2O_5.

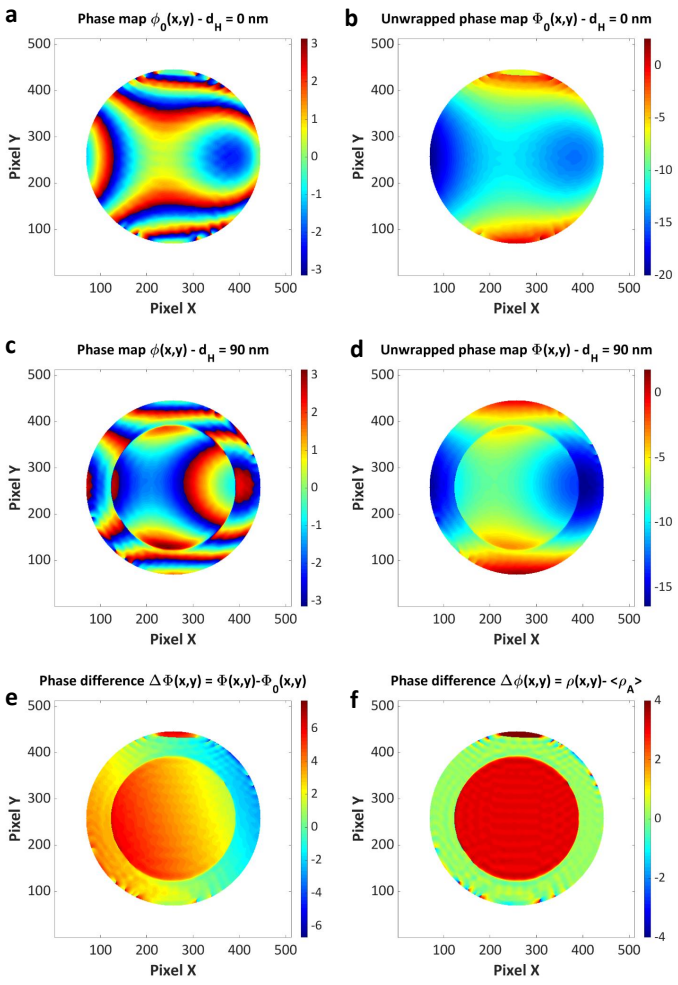

Fig. 8. False color representation of the phase maps used to extract the phase difference between the central zone and the reference annular zone (see text for more details).

By subtracting the unwrapped phase map recorded without coating from that recorded during deposition, the influence of the flatness error of the substrate is canceled (see Figure 8e). However, to simulate the effects of vibration, the tilt of the substrate is modified in our modeling program before each new acquisition: this explains the graded color changes observed in the central and annular zones. By subtracting the tilt value determined over the reference annular zone, this effect is canceled and the phase difference $\rho_C - \rho_A$ (see Figure 8f) is finally obtained, as expected.

4. Experimental results

The left of Figure 9 shows an overall view of the deposition machine with, on the top, the interferometric measurement system, and to the right of the same Figure, a closer view of the upper part of this experimental set-up. Note that the reference arm of the Michelson interferometer is folded using two plane mirrors at 45 degrees to satisfy dimensional constraints.

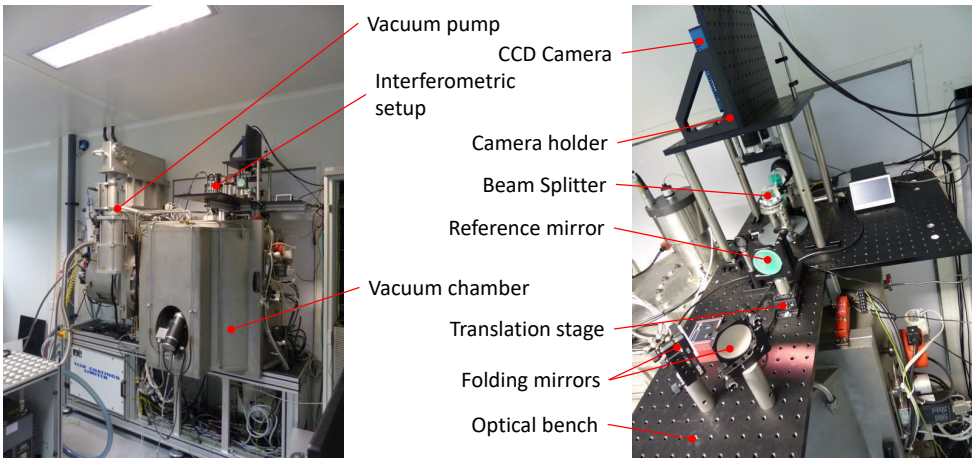

Fig. 9. Photographs of the experimental set-up (on the left, overall view of the deposition machine; on the right, a closer view of the upper part of the interferometric set-up).

4.1. Preliminary characterizations

Before applying this interferometric set-up to monitoring the deposition of a single layer, some preliminary tests were carried out to quantify its intrinsic performance.

The first test consists in using the motorized translation stage to scan the axial position of the reference mirror over a distance that allows the intensity of the echoes respectively associated with the reflection from the front face and from the rear face of a 2 mm thick bare silica substrate located in the substrate holder to be recorded. The result of this measurement is shown in Figure 10. Each maximum of visibility corresponds to a position of the reference mirror for which

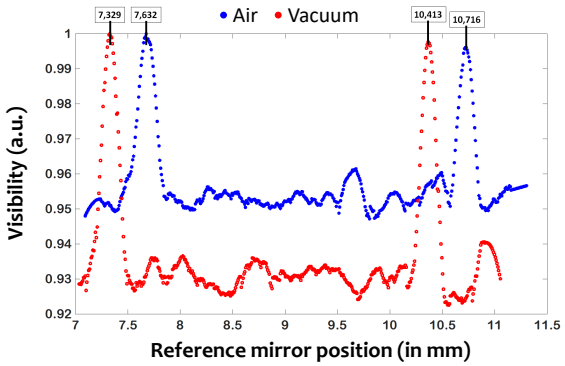

Fig. 10. Recording of the axial position of the echoes associated with the reflection from both faces of the substrate (blue dots, in air; red dots, in vacuum).

interference with an optical path difference of zero occurs. Consider the blue dots in the graph of

Figure 10, recorded when the deposition chamber is filled with air: the left maximum (z = 7.632 mm) corresponds to the reflection from the top face of the substrate, while the right maximum (z = 10.716 mm) is associated with the reflection from its bottom face. The distance between these two maxima, i.e. 3.084 mm, is in good agreement with the optical thickness of the substrate (2 mm). When the same recording is made under vacuum (red dots graph of Figure 10), the positions of both maxima are slightly shifted toward the low z values, in accordance with the refractive index decrease (approximately 3×10^{-4}) caused by an air-to-vacuum transition: indeed, this change causes a slight decrease in the optical path length of the Michelson arm whose substrate is the end-mirror. However, the distance between these two echoes is not changed (10.413 − 7.329 = 3.084 mm), since the optical thickness of the substrate is not affected by this air-to-vacuum transition. Finally, note that the full width at half maximum of each of these echoes is sufficiently narrow to guarantee that there is no overlap.

The second test consists in recording the time fluctuations of the phase difference $\Delta\phi$ measured over approximately 5 minutes on the same bare silica substrate in both static and dynamic configurations, i.e. with and without rotation of the substrate holder. The results are summarized in Tab.1, where Δ is the optical path difference associated with $\Delta\phi$ [$\Delta = \Delta\phi \times (\lambda/2\pi)$]. To

Configuration	$\langle\Delta\phi\rangle$ (radians)	$\sigma_{\Delta\phi}$ (radians)	$\langle\Delta\rangle$ (nm)	σ_{Δ} (nm)
static	0.005	0.015	0.7	2.0
dynamic	0.014	0.065	1.8	8.6

Table 1. Intrinsic Performance of the set-up in static and dynamic configurations

estimate the accuracy in term of deposited thickness, we have to divide these data by 2 (reflective configuration) and take into account the refractive index of the layer: this leads for instance to a measurement noise σ_d of about 2 nm in the case of a Ta_2O_5 layer.

4.2. Monitoring the deposition of a single layer

Figure 11shows two examples of results obtained during the deposition of a Ta_2O_5 layer.

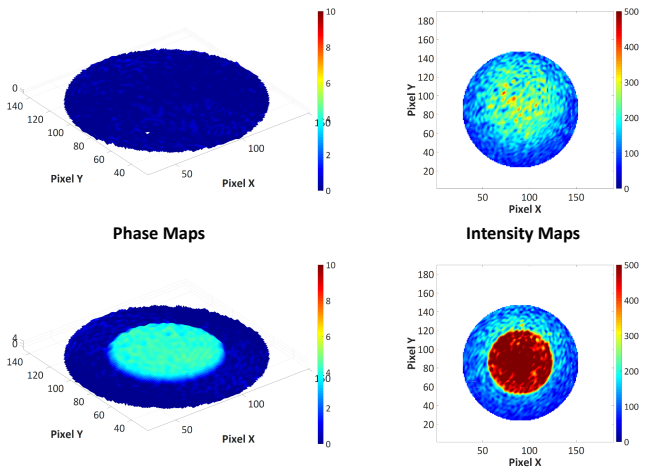

Fig. 11. Examples of phase and intensity maps recorded during the deposition of a Ta_2O_5 layer (on the top, d_H = 0 nm; on the bottom, $d_H \sim$ 50 nm).

The two top graphs correspond to the phase and intensity maps recorded just before deposition. The substrate holder is rotating and the deposition chamber is under vacuum. The two ion beams (sputtering and assistance) are ready to be activated. The two bottom graphs correspond to the same maps, but after deposition of a 50 nm thick Ta_2O_5 layer. The uniformity of the phase data recorded over both the central and annular zones, but also the level variation of the intensity recorded over the surface of the sample, reveal the Gaussian shape of the probe beam as well as its relatively narrow spectral bandwidth (speckle pattern). To overcome this difficulty, the modulus of the reflection coefficient is calculated using the following formula:

$$|r| = \frac{\langle S_1 \rangle_C}{\langle S_1 \rangle_A} \times \frac{\langle S_1 \rangle_{A,0}}{\langle S_1 \rangle_{C,0}} |r|_0 = \frac{\langle S_1 \rangle_C}{\langle S_1 \rangle_A} \times \frac{\langle S_1 \rangle_{A,0}}{\langle S_1 \rangle_{C,0}} \cdot \frac{n_s - 1}{n_s + 1} \tag{13}$$

where the quantities with subscript 0 correspond to the values recorded just before the start of deposition.

Figure 12 shows the change in the modulus and phase of the reflection coefficient with respect to time during the deposition of a half-wave silica layer onto a silica substrate.

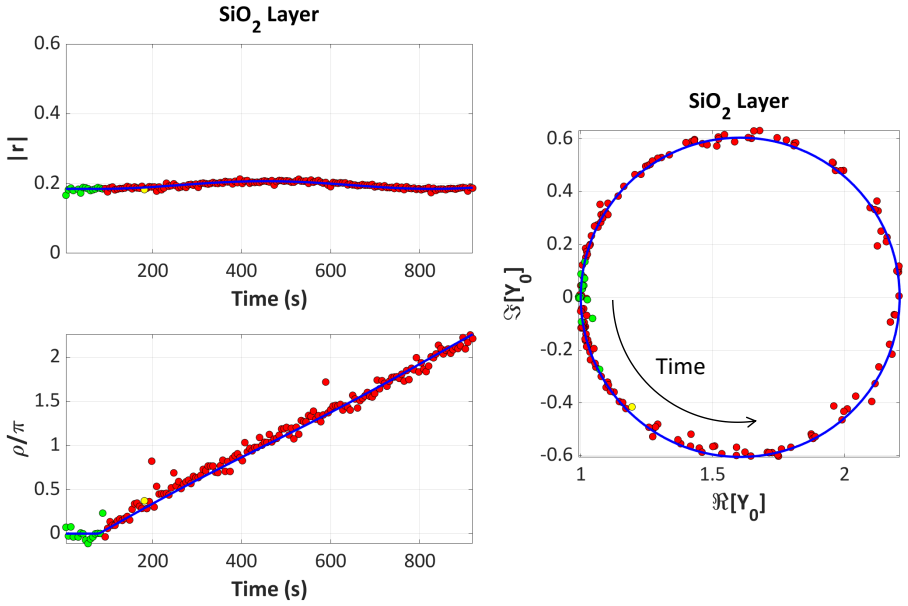

Fig. 12. Experimental data recorded during the deposition of a half-wave silica layer onto a silica substrate (see text for more details).

The red dots correspond to measurement results, namely the modulus of r and its argument ρ divided by π. The green dots also correspond to experimental results, but the color change is used simply to identify the acquisitions performed before the start of the layer deposition. Moreover, by inverting relation (6), the admittance Y_0 can be derived from the reflection coefficient r, i.e.

$$Y_0 = n_s \left(\frac{1 - r}{1 + r} \right) \tag{14}$$

The result of this calculation is presented on the right of Figure 12 as a trajectory in the complex plane (admittance locus). Finally, on these three graphs the blue line corresponds to a theoretical fit, based on relation (7), in which the only free parameters are the refractive index of the layer (n_1), the deposition rate (v), assumed constant, and the time value t_0 corresponding to the start of

the layer deposition. Consequently, we have:

$$d_1(t) = \begin{cases} 0 & \text{if } t \leqslant t_0 \\ v(t - t_0) & \text{if } t \geqslant t_0 \end{cases} \tag{15}$$

The fitting process provides the following results: $t_0 = 80$ s, $v = 0.374$ nm/s, and $n_1 = 1.4865$, the agreement between experimental data and theoretical fit is excellent. Moreover, the deposition rate and the refractive index are comparable with those obtained a few months ago [$v = 0.3364$ nm/s, $n_1 = 1.4837$] on the same deposition machine using another method [12].

The results obtained with the same approach during the deposition of a half-wave tantala layer on a silica substrate are shown in Figure 13. Again, the agreement between experimental results

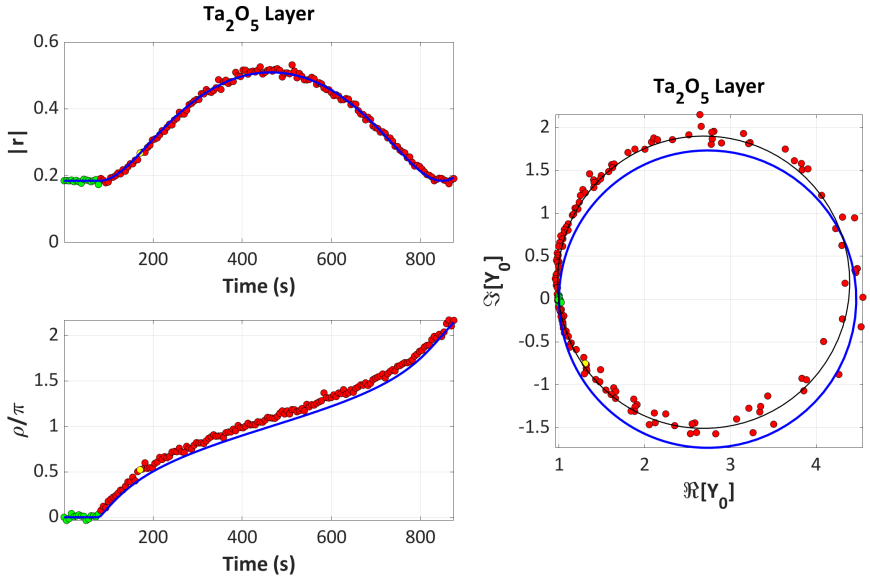

Fig. 13. Experimental data recorded during the deposition of a half-wave tantala layer on a silica substrate (see text for more details).

and theoretical fit for the modulus of the reflection coefficient is very satisfactory, but there is also a slight discrepancy in the phase term (about 0.25 radians). This small difference is notably visible on the admittance locus graph (right of Figure 13) where the center of the blue circle clearly does not appear to be in the right place, even though its radius seems correct. Adding 0.25 radians to the theoretical phase values shifts the model data (thin black circle) to the right place with respect to the experimental data. We still have no satisfactory explanation for this discrepancy. Note that the refractive index and deposition rate values (respectively, 2.1137 and 0.255 nm/s) are in good agreement with the results of previous measurements [8].

5. Discussion and conclusion

5.1. Discussion

This interferometric approach allows the growth of a single layer to be monitored through the temporal change of the admittance Y_0 in the complex plane. The trajectory shape shows that the accuracy of the deposition cut should be nearly independent of the layer thickness.

To confirm this preliminary conclusion, we consider multilayer stacks, such as a quarter-wave mirror, as illustrated by Figure 14. High index layers (tantala) correspond to red circles, low

index layers (silica) to blue circles; green (respectively yellow) dots are used to identify the start (respectively the end) of the deposition. Note that phase variations recorded during the deposition of a layer become lower and lower, which can progressively decrease the signal-to-noise ratio of the measurements for quarter-wave mirrors with large number of HL pairs.

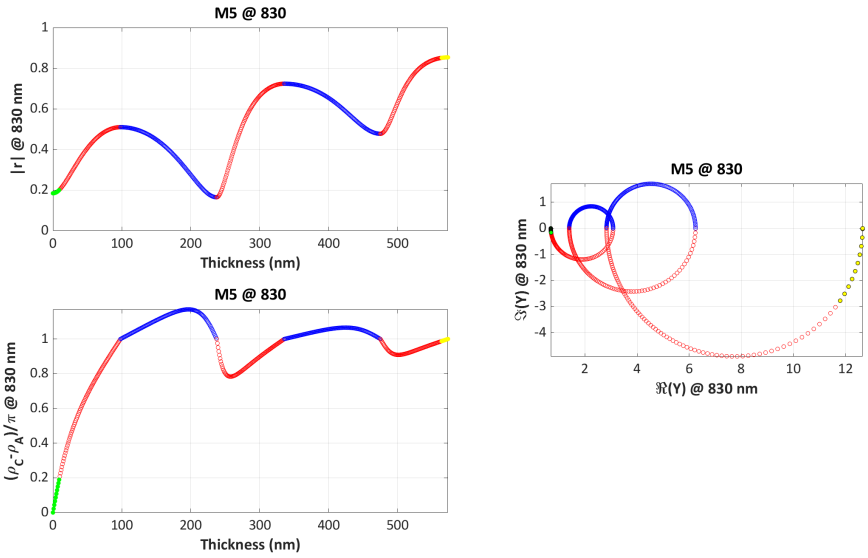

Fig. 14. Theoretical data recorded during the deposition of a quarter-wave mirror (tantala/silica) onto a silica substrate (see text for more details).

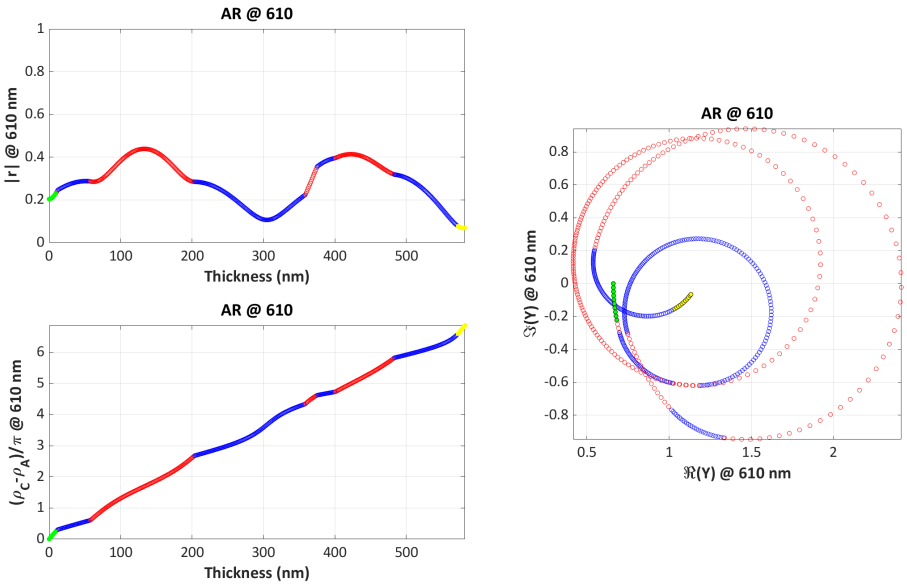

Fig. 15. Theoretical data recorded during the deposition of an 8-layer antireflective coating onto an N-BK7 substrate.

If we now consider the case of an 8-layer antireflective coating (see Figure 15) that includes some very thin layers with thicknesses less than 25 nm, we see that the phase variations are

mostly linear throughout the stack deposition, while the dimensions of the admittance locus are approximately the same as those recorded during the deposition of a half-wave silica layer. The same conclusion can be formulated for monitoring the adaptation layer inserted between the two cavities of a Fabry-Perot bandpass filter: the use of interferometric monitoring provides a real advantage with respect to methods based only on intensity measurements.

5.2. Conclusion

We have demonstrated that the use of an interferometric scheme can provide useful information for the *in situ* monitoring of the deposition of transparent layers. The implementation of a self-referenced scheme allows accurate measurements to be obtained despite the severe constraints created by the thermal and vibrational environment, and nothing appears to prevent this method from being extended to the monitoring of thin absorbing or metallic layers. However, it would be necessary to add a motorized sub-assembly using e.g. a Risley prism pair to provide a dynamic alignment capability of the probe beam with respect to the substrate (as stressed above, the tilt angle between the reference mirror and the substrate must remain between 0.005 radians and 0.01 radians).

Moreover, it is surely possible to implement simultaneously optical broadband monitoring (we have successfully carried out some preliminary tests in this direction) so as to mix intensity and phase measurements in this way.

In addition, the use of low coherence interferometry allows easy implementation of some other on-line measurements, such as *in situ* stress monitoring (measurement of the radius of curvature of the rear face of the substrate), or estimating the uniformity of the deposited layers and even a real time measurement of the temperature of the substrate.

Acknowledgments

This work was carried out within the LabTOP (Laboratoire commun de Traitement OPtique des surfaces), a research cooperation agreement between the Institut Fresnel (Aix-Marseille Univ, CNRS, Centrale Marseille) and CILAS Ariane Group.

Disclosures

The authors declare no conflicts of interest.

References

1. A. V. Tikhonravov, M. K. Trubetskov, T. V. Amotchkina, "Optical monitoring strategies for optical coating manufacturing," in *Optical Thin Films and Coatings: From Materials to Applications, 2nd edition*, A. Piegari and F. Flory, eds. (Woodhead Publishing Ltd, 2018), pp. 65-99.
2. C. C. Lee, K. Wu, S. H. Chen, and S. J. Ma "Optical monitoring and real time admittance loci calculation through polarization interferometer," Opt. Express **15**, 17536–17541 (2007).
3. K. Wu, M. C. Li, J. C. Wyant, N. J. Brock, B. Kimbrough, and C. C. Lee "Optical Admittance Monitor through a Dynamic Interferometer," in *Optical Interference Coating*, OSA Technical Digest (Optical Society of America, 2010), paper TuC5.
4. K. Wu, C. C.Lee, N. J. Brock, and B. Kimbrough, "Multilayer thin-film inspection through measurements of reflection coefficients," Opt. Lett. **36**, 3269–3271 (2011).
5. 4D Technology, https://www.4dtechnology.com/products/dynamic-interferometry/.
6. N. Brock, J. Hayes, B. Kimbrough, J. Millerd, M. North-Morris, M. Novak and J. C. Wyant, "Dynamic Interferometry," Proc. SPIE **5875**, 58750F (2005).
7. P. Picart and J. C. Li, *Digital holography* (ISTE and John Wiley & Sons, 2012).
8. M. Lequime, S. L. Nadji, D. Stojcevski, C. Koc, C. Grèzes-Besset, and J. Lumeau, "Determination of the optical constants of a dielectric layer by processing *in situ* spectral transmittance measurements along the time dimension," Appl. Opt. **56**, C181–C187 (2017).
9. H. A. Macleod, *Thin-Film Optical Filters*, 5^{th} Edition (CRC Press, 2018).
10. C. Amra, M. Lequime, and M. Zerrad, *Electromagnetic Optics in Thin-Film Coatings* (Cambridge University Press, 2020).

11. M. A. Herraez, D. R. Burton, M. J. Lalor, and M. A. Gdeisat, "Fast two-dimensional phase unwrapping algorithm based on sorting by reliability following a noncontinuous path," Appl. Opt. **41**, 7437–74447 (2002).
12. S. L. Nadji, M. Lequime, T. Begou, C. Koc, C. Grèzes-Besset, and J. Lumeau, "Use of a broadband monitoring system for the determination of the optical constants of a dielectric bilayer," Appl. Opt. **57**, 877–883 (2018).